Nanoscale

COMMUNICATION

View Article Online
View Journal | View Issue

Cite this: *Nanoscale*, 2020, **12**, 10977

Received 21st February 2020,
Accepted 29th April 2020

DOI: 10.1039/d0nr01496f

rsc.li/nanoscale

Gradient phosphorus-doping engineering and superficial amorphous reconstruction in $NiFe_2O_4$ nanoarrays to enhance the oxygen evolution electrocatalysis†

Wei Zong,‡[a] Dewei Rao, ‡[b] Hele Guo,[a] Yue Ouyang,[a] Yue-E. Miao, [a] Wei Wang, [c] Jing Wang, [d] Feili Lai *[e] and Tianxi Liu*[a]

A better solid–liquid–gas three-phase boundary is vital for low energy cost oxygen evolution reaction (OER), making the designed regulation of interfacial atmosphere necessary. Herein, we find that the OER electrocatalysis can be dramatically improved by synergistically forming disordered electronic structures and superficial amorphous layers, as superficial oxyhydroxide, phosphorus-doped $NiFe_2O_4$ nanoarrays on nitrogen-doped carbon nanofibers (OP-$NiFe_2O_4$/NCNFs). Unveiled by the depth-profiling analysis from the X-ray photoelectron spectroscopy, the contents of phosphorous doping in the OP-$NiFe_2O_4$ nanoarrays change dynamically from outside to inside due to its *in situ* superficial reconstruction into the oxyhydroxide layer, thereby accelerating electron transfer between heterogeneous phases. As revealed by density functional theory calculations, this amorphous oxyhydroxide layer and dynamically varied phosphorous content would positively shift the d-band center of the $NiFe_2O_4$-related compounds, leading to lower adsorption energy towards water molecule. Thus, the OP-$NiFe_2O_4$/NCNF electrocatalyst displays a low overpotential of 260 mV at a current density of 10 mA cm^{-2} and a small Tafel slope of 44.8 mV dec^{-1} in an alkaline medium.

Introduction

Due to a series of negative consequences caused by the increasing consumption of fossil fuels,[1–3] it is highly imperative to develop alternative sustainable energy technologies, such as water splitting, CO_2 reduction, and nitrogen reduction reactions.[4–9] However, the oxygen evolution reaction (OER), suffering from the nature of sluggish kinetics of the four proton-coupled electron transfer process, has become efficiency-determining step and main bottleneck of overall efficiency of water splitting.[10–15] Therefore, it has already been an inevitable tendency to exploit highly-efficient and durable OER electrocatalysts for the water splitting system. To date, iridium/ruthenium-based (IrO_2/RuO_2) compounds are the most active OER electrocatalysts but their practical scale-up application is still greatly hindered on the account of scarcity and high cost.[16,17]

Earth-abundant first-row 3d transition-metal-based compounds have been demonstrated as promising water oxidation electrocatalysts, including transition-metal hydroxides,[18,19] oxides,[20] sulfides,[21] selenides,[22] and phosphides.[23] Among them, $NiFe_2O_4$ has been regarded as a potential OER electrocatalyst owing to its superior catalytic activity and excellent stability in an alkaline medium. However, $NiFe_2O_4$ consistently suffers from sluggish OER kinetic processes due to poor electrical conductivity, making it necessary to modulate the inherent electronic property. Among all possible methods, atomic-level modifications (such as heteroatom-doping engineering,[24,25] structural strain effect,[26,27] or vacancy engineering[28–30]) represent the most prospective ones to enhance the electrical conductivity of $NiFe_2O_4$. For example, non-metal heteroatoms possess extraordinary bonding ability with both nickel and iron atoms to make the electrons transfer faster between the heterogeneous phases, leading to the breakthrough of the sluggish OER kinetic processes in the $NiFe_2O_4$ bulk. Typically, phosphorus has not only vacant 3d orbitals but also lone-pair electrons in 3p orbitals, making it an intriguing candidate to regulate the local charge density and the adsorption energy of reactive species.[31–33]

[a]*State Key Laboratory for Modification of Chemical Fibers and Polymer Materials, College of Materials Science and Engineering, Innovation Center for Textile Science and Technology, Donghua University, Shanghai 201620, P. R. China. E-mail: txliu@dhu.edu.cn*
[b]*School of Materials Science and Engineering, Jiangsu University, Zhenjiang, Jiangsu 212013, P. R. China*
[c]*Beijing Key Laboratory of Bio-inspired Energy Materials and Devices, School of Space and Environment, Beihang University, Beijing, 100191, PR China*
[d]*School of Chemical Engineering and Energy, Zhengzhou University, Zhengzhou, Henan 450001, P. R. China*
[e]*Department of Chemistry, KU Leuven, Celestijnenlaan 200F, Leuven 3001, Belgium. E-mail: feili.lai@kuleuven.be*

†Electronic supplementary information (ESI) available. See DOI: 10.1039/d0nr01496f

‡These authors contributed equally to this work.

In general, the oxygen evolution reaction occurs at a three-phase boundary of solid electrode, aqueous electrolyte, and oxygen gas, which indicates the superficial chemical environment of the solid electrode is vitally important to enhance the electrocatalysis. Under a high working potential (commonly over 1.5 V *vs.* RHE), in fact, it has been proved that the majority of OER electrocatalysts would undergo a phase transformation or structural reconstruction, which can offer highly active phases for the oxygen evolution reaction.[34] However, it is still imperative to study the definite identification of real active species for the OER process. Recently, emerging studies report that the efficient active phase in the transition-metal phosphides, sulfides, and selenides is likely to be the as-formed superficial (oxy)hydroxides or oxides during the OER process. Xu *et al.* reported that nickel iron diselenide nanosheets were transformed into corresponding hydroxides under oxygen-evolution conditions, which showed a much more intensive OER activity.[35] As demonstrated by Zhang *et al.*, this would originate from the evident and irreversible phase transformation of the metal phosphides as strong anodic oxidation in the OER potential range.[36] However, this transformation process is sluggish in spinel-type oxide counterparts owing to their stable crystalline structures.[37] To our knowledge, it is still difficult to make the structure evolution in transition-metal-based oxide derivatives much clearer during the OER process, particularly those combining with suitable non-metal heteroatom doping as phosphorus.[38–40]

Herein, we prepared the phosphorus-doped $NiFe_2O_4$ nanoarrays on nitrogen-doped carbon nanofibers (P-$NiFe_2O_4$/NCNF). During the electrochemical activation process, we found that a unique superficial self-reconstruction occurs on the surface of P-$NiFe_2O_4$/NCNF from highly crystalline $NiFe_2O_4$ oxides into amorphous oxyhydroxides. Density functional theory (DFT) calculations revealed that the phosphorous incorporation and superficial amorphous oxyhydroxide have the synergistic effect, which could not only activate the $NiFe_2O_4$ electrocatalyst with the regulated d-band, but also facilitate the adsorption of water with low energy. As a result, the as-obtained OP-$NiFe_2O_4$/NCNF delivers a low overpotential of 260 mV at a current density of 10 mA cm^{-2} as well as a low Tafel slope of 44.8 mV dec^{-1} for OER in 1 M KOH electrolyte. Therefore, the rational surface engineering could efficiently modulate the local electron density and afford fundamental insights into the catalytic origin linked to self-reconstruction of the OER electrocatalysts.

Results and discussion

As shown in the Fig. 1a, the overpotential for the oxygen evolution reaction process by phosphorus-doped $NiFe_2O_4$ nanoar-

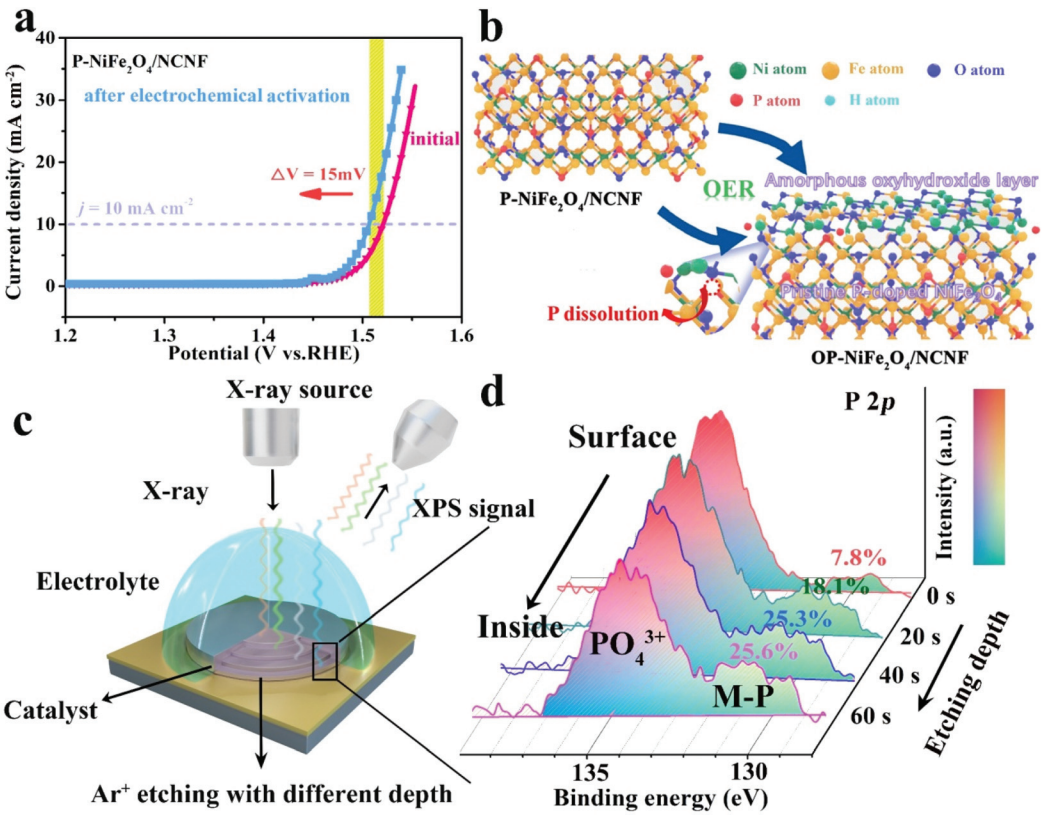

Fig. 1 (a) Polarization curves of P-$NiFe_2O_4$/NCNF tested in the first cycle and after the electrochemical activation process. (b) Proposed *in situ* surface self-restructuration from the as-prepared oxides to amorphous oxyhydroxides. (c) Schematic of the depth-profiling XPS(DP-XPS) experimental setup, and (d) corresponding XPS core levels of P 2p with different Ar^+ etching time periods.

rays on the nitrogen-doped carbon nanofiber (P-$NiFe_2O_4$/NCNF) electrocatalyst greatly reduced after electrochemical activation at a current density of 10 mA cm^{-2}, which is not observed in the non-phosphorus-doped electrode of $NiFe_2O_4$/NCNF (ESI, Fig. S1†). This electrochemical behavior may originate from the *in situ* self-reconstruction of P-$NiFe_2O_4$/NCNF into new active species as an amorphous oxyhydroxides layer (Fig. 1b), which is deemed to be a dynamical self-optimization process and the evolution for a stable catalytic surface for the OER. More importantly, the difference between P-$NiFe_2O_4$/NCNF and $NiFe_2O_4$/NCNF indicates that the phosphorus-doped atoms in P-$NiFe_2O_4$ would trigger the *in situ* self-reconstruction. Furthermore, the depth-profiling X-ray photoelectron spectroscopy technique (DP-XPS) (Fig. 1c) was used to investigate the chemical and structural evolution of the P-$NiFe_2O_4$/NCNF during the electrochemical activation. According to the P 2p spectra shown in Fig. 1d and S2 (ESI†), the corresponding peaks can be divided into two species of PO_4^{3+} bonds (134.1 eV) and metal–phosphorus (M–P) bonds (129.9 eV). As the etching time increases from 0 to 60 s, the content of the M–P bond increases gradually, demonstrating a dynamic change in the OP-$NiFe_2O_4$ nanosheet from outside to inside. Also, the P 2p spectrum of P-$NiFe_2O_4$/NCNF before electrochemical activation has been added for comparison (ESI Fig. S3†). The low M–P content in the surface of the phosphorus-doped $NiFe_2O_4$ introduces abundant heterogeneous phases with possibly an unstable structure, which would facilitate *in situ* self-reconstruction from the highly crystalline $NiFe_2O_4$ oxides to the amorphous oxyhydroxide layer. As displayed in the above polarization curves, the enhanced OER performance would originate from the as-formed amorphous oxyhydroxide layer.

Therefore, the superficial oxyhydroxide, phosphorus-doped $NiFe_2O_4$ nanoarrays on nitrogen-doped carbon nanofibers (OP-$NiFe_2O_4$/NCNFs) can be prepared as the steps shown in the schematic (ESI, Fig. S4†). In detail, $NiFe_2O_4$ nanoarrays were directly covered on the surface of NCNF after the hydrothermal and controlled annealing process of NiFe-LDH (ESI, Fig. S5†) which can avoid the agglomeration of the bulk $NiFe_2O_4$ (ESI, Fig. S6†) for expediting the electron transport. In addition, P-$NiFe_2O_4$/NCNF was synthesized through the phosphorus-doped method. Then, the surface of P-$NiFe_2O_4$/NCNF was transformed to amorphous oxyhydroxides in the subsequent electrochemical activation as OP-$NiFe_2O_4$/NCNF. Fig. 2a shows the XRD patterns of OP-$NiFe_2O_4$/NCNF, $NiFe_2O_4$/NCNF and $NiFe_2O_4$ bulk, which represent almost similar profiles with five characteristic peaks at 2θ = 30.3°, 35.7°, 43.3°, 57.3°, and 62.9° assigned to (220), (311), (400), (511), and (440) lattice planes of the $NiFe_2O_4$ phase (JCPDS Card no. 10-0325), respectively. These results confirm that neither the phosphorus-doping engineering nor the electrochemical activation would impact the main crystal structure of $NiFe_2O_4$ as the

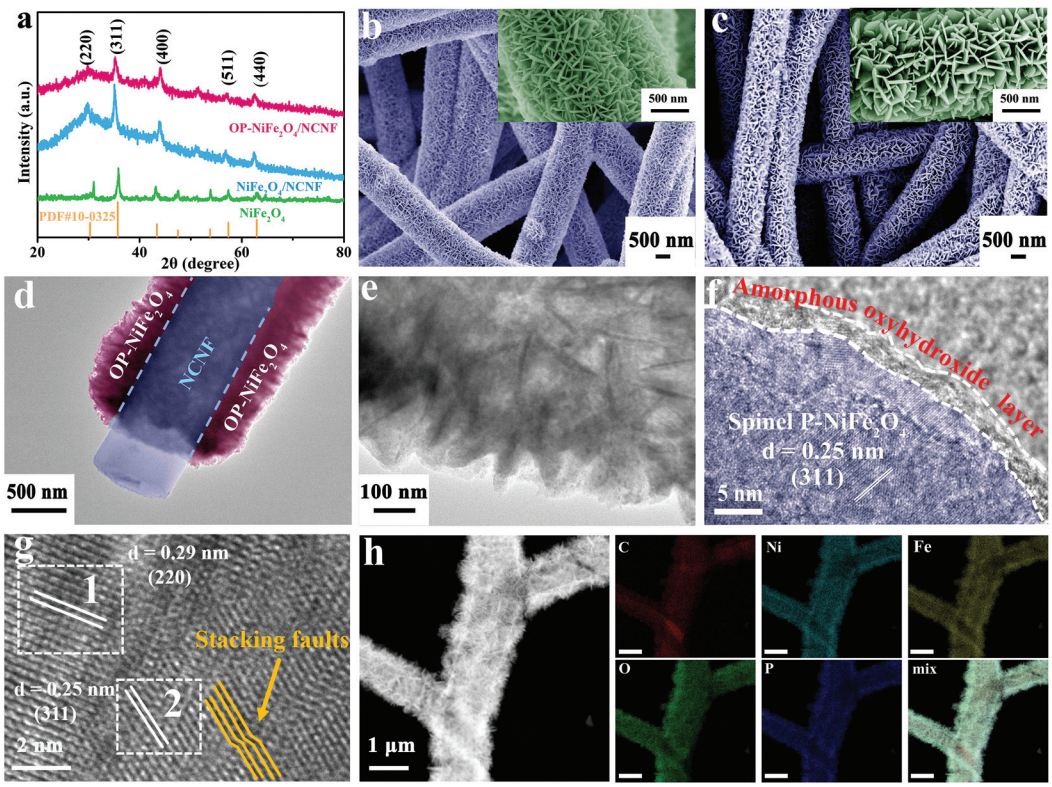

Fig. 2 (a) The XRD patterns of OP-$NiFe_2O_4$/NCNF, $NiFe_2O_4$/NCNF and $NiFe_2O_4$ bulk. The FESEM images of (b) $NiFe_2O_4$/NCNF, and (c) OP-$NiFe_2O_4$/NCNF. Inset: under a high magnification. (d and e) The TEM images of OP-$NiFe_2O_4$/NCNF. (f and g) The HRTEM image of OP-$NiFe_2O_4$/NCNF. (h)The STEM-EDS elemental mapping images of OP-$NiFe_2O_4$/NCNF. Scalebar: 1 μm.

slight doping of phosphorous atoms and generation of the oxyhydroxide layer. The scanning electron microscopy (SEM) images reveal that the quasi-vertically $NiFe_2O_4$ nanoarrays are uniformly anchored on the surface of NCNF, represented as $NiFe_2O_4$/NCNF (Fig. 2b). Meanwhile, the OP-$NiFe_2O_4$ nanoarrays (Fig. 2c) are well maintained on NCNFs, indicating that the electrochemical activation process would not affect the nanoarray morphology significantly. As shown in Fig. 2d, the transmission electron microscopy (TEM) image demonstrates that the OP-$NiFe_2O_4$ nanoarrays are closely connected with the NCNF. Meanwhile, the successful formation of the amorphous oxyhydroxide layer confined on the surface of the P-doped $NiFe_2O_4$ nanosheet is demonstrated by the TEM image (Fig. 2e). In detail, the inside OP-$NiFe_2O_4$ shows a well-crystallized structure with an inter-planar distance of 0.25 nm, corresponding to the (311) plane of the $NiFe_2O_4$ phase, while the outside OP-$NiFe_2O_4$ successfully transformed into amorphous oxyhydroxide layers revealed by the high-resolution transmission electron microscopy (HRTEM) image (Fig. 2f). As seen at a higher magnification, another preferred (220) direction can also be observed in the marked region of Fig. 2g with an inter-planar distance of 0.29 nm. Differing from the high crystallinity of undoped $NiFe_2O_4$ (ESI, Fig. S8†), the zigzag lattice in the P-doped $NiFe_2O_4$ indicates the existence of stacking faults deriving from the unmatched sizes between phosphorous and the oxygen atoms.[41,42] The substituted phosphorous atoms in transition-metal oxide structure are of benefit to trigger the formation of new active sites during the electrochemical activation.[31] Energy-dispersive X-ray spectroscopy (EDS) of high-angle annular dark-field scanning transmission electron microscopy (HAADF-STEM) (Fig. 2h) reveals a homogeneous spatial distribution of the elements Ni, Fe, O and P on the surface of the carbon nanofibers as a fibrous integrity.

To experimentally investigate the electronic structure evolution in OP-$NiFe_2O_4$/NCNF during the electrochemical activation process, DP-XPS combined with Ar^+ etching sources was carried out again. The binding energies at approximately 853.6 and 856.2 eV in the Ni 2p spectra (Fig. 3a) are assigned to Ni^{2+} $2p^{3/2}$ and Ni^{3+} $2p^{3/2}$, respectively,[43,44] while the ratio of Ni^{3+}/Ni^{2+} reduced gradually when etching time increased from 0 to 60 s. This is because the Ni element in the oxyhydroxide layers mainly exists in a high valence state of Ni^{3+} as NiOOH, which is made up of weakly interacting hydroxide layers that permit the intercalation of more anions and water molecule for favorable active sites towards the OER.[45] Fig. 3b shows two peaks at binding energies of 708.3 and 711.5 eV in the OP-$NiFe_2O_4$/NCNF, which can be indexed to Fe^{2+} $2p^{3/2}$and Fe^{3+} $2p^{3/2}$,[46,47] respectively. Similarly, the DP-XPS spectra of Fe indicate that

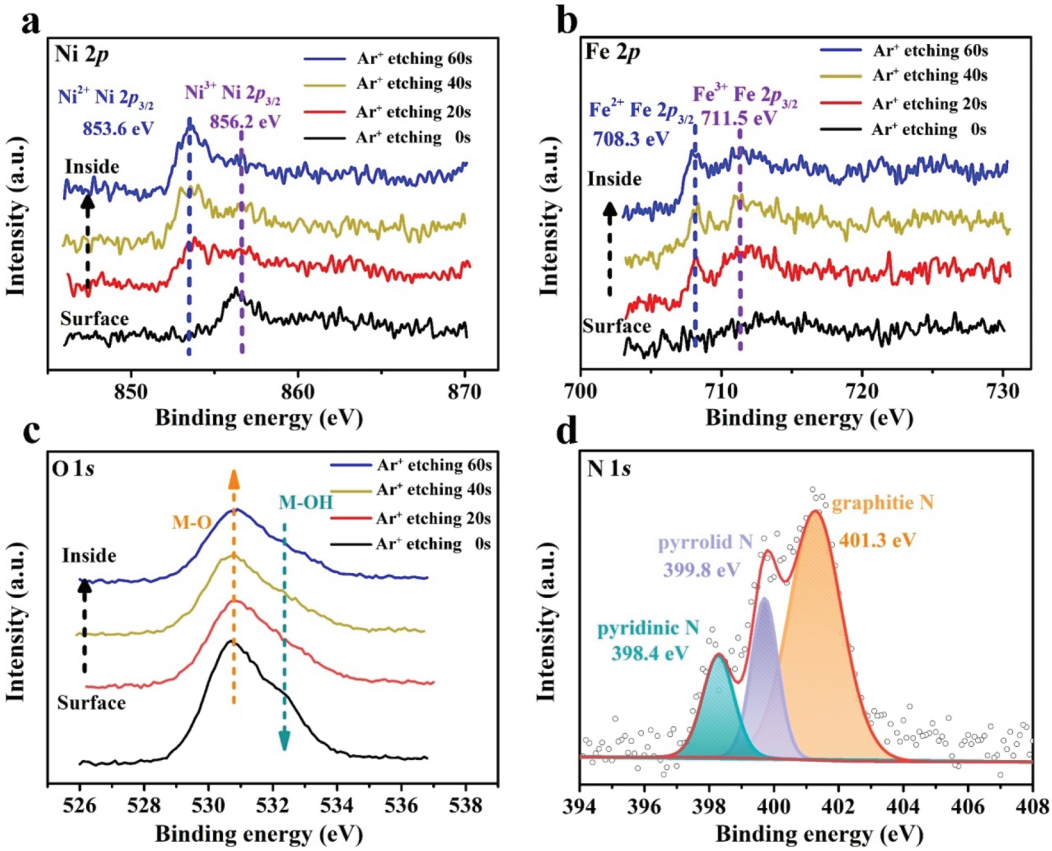

Fig. 3 XPS core levels of (a) Ni 2p, (b)Fe 2p, (c) O 1s of OP-$NiFe_2O_4$/NCNF with different Ar^+ etching time periods. (d) XPS core levels of N 1s for OP-$NiFe_2O_4$/NCNF.

high valence state Fe^{3+} is the dominant valence state on the surface of OP-$NiFe_2O_4$/NCNF. As shown in Fig. 3c, the O 1s high resolution spectra can be divided into two main peaks at 530.8 and 532.4 eV, corresponding to the metal–oxygen (M-O) and metal-hydroxide (M–OH) bonds, respectively.[48] The ratio of M–OH/M–O decreases significantly with continuous Ar^+ etching treatment, demonstrating that the superficial M–O bonds are successfully replaced by superficial amorphous oxyhydroxides after the electrochemical activation process. In addition, the N 1s spectrum of OP-$NiFe_2O_4$/NCNF (Fig. 3d) can be deconvoluted into pyridinic-N (398.4 eV), pyrrolic-N (399.8 eV) and graphitic-N (401.3 eV), respectively, which would bond with the OP-$NiFe_2O_4$ nanoarray and maintain the structural stability.[49] Moreover, the nitrogen adsorption–desorption isotherms of OP-$NiFe_2O_4$/NCNF and $NiFe_2O_4$ powder are provided in Fig. S9a (ESI†). The OP-$NiFe_2O_4$/NCNF displays a higher Brunauer–Emmett–Teller (BET) specific surface area (SSA) of 38.8 $m^2\ g^{-1}$ as compared to the $NiFe_2O_4$ powder (12.8 $m^2\ g^{-1}$). As per the pore size distribution curves shown in Fig. S9b (ESI†), the OP-$NiFe_2O_4$/NCNF exhibits micro-/mesoporous structures with pore diameters mainly centered at 8–16 nm. The difference between the specific surface areas of OP-$NiFe_2O_4$/NCNF and $NiFe_2O_4$ powder demonstrates that the 3D network of NCNF is beneficial for solving the severe aggregation of $NiFe_2O_4$ bulk and thus endowing more electrochemical active sites for the OER process.

The OER activity of all the samples was investigated in O_2-saturated 1 M KOH. Fig. 4a shows the typical linear sweep voltammetric (LSV) curves. The OP-$NiFe_2O_4$/NCNF requires a low overpotential (η) of 260 mV at a current density of 10 mA cm^{-2}, which is 99 and 121 mV lower than those of the $NiFe_2O_4$/NCNF and $NiFe_2O_4$, respectively. Further revealed in Fig. 4b, the Tafel slope of OP-$NiFe_2O_4$/NCNF (44.8 mV dec^{-1}) is much lower than those of the $NiFe_2O_4$/NCNF (90.1 mV dec^{-1}) and $NiFe_2O_4$ (113.2 mV dec^{-1}), implying a favorable OER kinetics for the OP-$NiFe_2O_4$/NCNF. The overpotential and Tafel slope of OP-$NiFe_2O_4$/NCNF are also much more superior to most of the reported transition-metal-based electrocatalysts for OER (ESI, Table S2†). To further illuminate the enhanced OER performance of OP-$NiFe_2O_4$/NCNF, double layer capacitances (C_{dl}) were applied to estimate the electrochemical active surface area (ECSA) of different samples, which were tested by the cyclic voltammetry (CV) method in the non-faradaic reaction range (ESI, Fig. S11†). Fig. 4c shows that the C_{dl} of OP-$NiFe_2O_4$/NCNF is 16.4 mF cm^{-2}, which is higher than that of the $NiFe_2O_4$/NCNF (10.7 mF cm^{-2}). As manifested by the correlation between the overpotential at 10 mA cm^{-2} and turnover frequency (TOF) of the different samples in Fig. 4d, the reduced overpotential for the OP-$NiFe_2O_4$/NCNF can be corresponding to the increased TOF with more active sites for the OER process. Specifically, the TOF value of OP-$NiFe_2O_4$/NCNF is calculated to be 0.0389 s^{-1} at the overpotential of 350 mV, which is 11.1 and 22.8 times higher than that of $NiFe_2O_4$/NCNF (0.0035 s^{-1}) and $NiFe_2O_4$ (0.0017 s^{-1}), indicating the highest atom-utilization efficiency of the OP-$NiFe_2O_4$/NCNF among these three electrocatalysts. Moreover, electrochemical impedance spectroscopic (EIS) analysis is performed to study the interfacial properties at the solid–liquid–gas three-phase boundary of the electrode, electrolyte, and oxygen gas. Fig. 4e manifests that the OP-$NiFe_2O_4$/NCNF possesses much lower charge-transfer resistance (R_{ct} = 9.1 Ω) as compared to those of $NiFe_2O_4$/NCNF (R_{ct} = 22.7 Ω) and $NiFe_2O_4$ (R_{ct} = 119.8 Ω), indicating its fastest charge transfer ability and accelerated catalytic kinetics after applying phosphorus-doping engineering. In addition, the polarization curve of the OP-$NiFe_2O_4$/NCNF after 1000 cycles nearly overlaps with the original curve with approximately 100% faradaic efficiency (Fig. 4f), demonstrating a satisfactory stability over a long-period of OER electrolysis of OP-$NiFe_2O_4$/NCNF. Moreover, the OP-$NiFe_2O_4$/NCNF composites can still maintain the morphology and chemical composition after being tested for long-term cycles as revealed by the TEM image and XPS data (ESI Fig. S12 and S13†). As shown in Fig. 4g, the doped phosphorus in $NiFe_2O_4$ would slightly change the crystallinity and disorder the electronic structures, as well as trigger the *in situ* superficial self-reconstruction of the $NiFe_2O_4$ into amorphous oxyhydroxide layers, which are beneficial in facilitating the electron transport between inside oxides and outside active species. The emergence of superficial amorphous oxyhydroxide layers facilitates the electrostatic adsorption of H_2O molecules or OH^- ions, which is regarded as the bottleneck to boost the oxygen evolution reaction in alkaline electrolyte accordingly.

Density functional theory (DFT) calculations were carried out to understand the impacts of superficial oxyhydroxide layers and doped phosphorus atoms on the electrocatalytic performance. The projected density of states (PDOS) of pristine $NiFe_2O_4$, phosphorus-doped $NiFe_2O_4$ (P-$NiFe_2O_4$) and $NiFe_2O_4$ with amorphous oxyhydroxide layer ($NiFe_2O_4$-OH) were firstly calculated as presented in Fig. 5a–c. It is clear that the d electrons of Fe distributed near the Fermi level, however, are not likely to form an effective interaction with the O 2p orbital. The Fe 3d orbital and O 2p orbital hybridized in energy about −3 eV *vs.* Fermi level and as a result the O-contained species would be strongly adsorbed at the Fe sites, which is beneficial for further reaction during the OER processes. Meanwhile, the change of charge densities around the Fe atom and neighboring metal atoms are shown in Fig. 5d–f, indicating the degree of charge polarization. It is clear that the change for Fe of pristine $NiFe_2O_4$ is smaller than that of P-$NiFe_2O_4$ and $NiFe_2O_4$-OH, indicating that the charge transfer from Fe of pristine $NiFe_2O_4$ is harder than other samples, which will reduce the adsorption of H_2O. As a result, the adsorption energy of $NiFe_2O_4$ is lowest (−0.820 eV) when compared to P-$NiFe_2O_4$ (−1.499 eV) and $NiFe_2O_4$-OH (−0.900 eV) (Fig. 5h). More than that, the strong adsorption of electrons to Fe will impede the kinetics of electrons, which greatly influence the OER reactions with election-transfer processes. Impressively, as shown in Fig. 5g, we found that the d-band center of the P-$NiFe_2O_4$ and $NiFe_2O_4$-OH model are −1.24 and −1.21 eV, much closer to the Fermi level when compared to that of the pristine $NiFe_2O_4$ model (−1.49 eV). The d-band center is closer to the Fermi level, which indicates that the anti-bonding energy states are enhanced when bonding with the OER-intermedi-

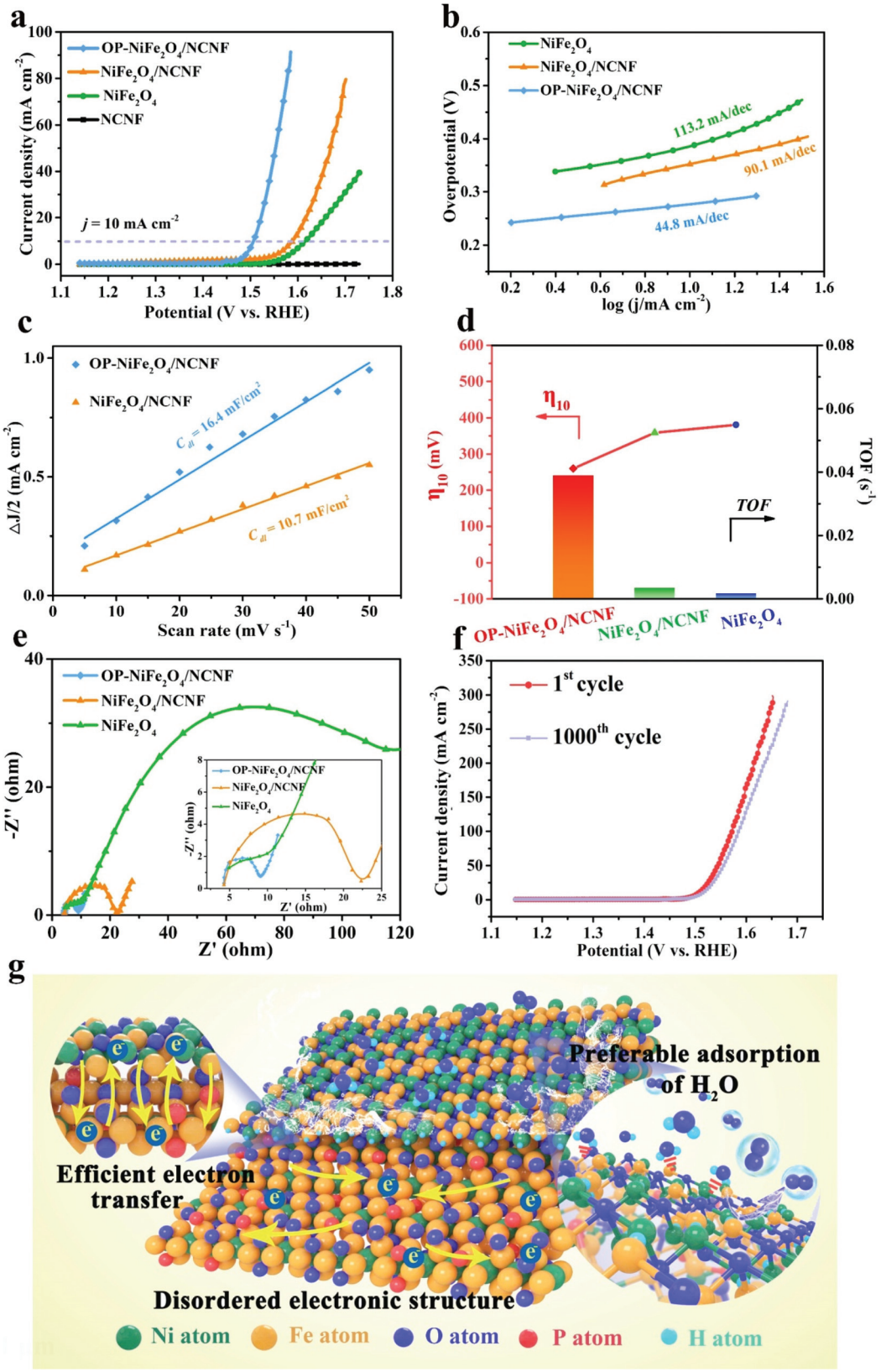

Fig. 4 (a) Polarization curves, and (b) Tafel plots of OP-$NiFe_2O_4$/NCNF, $NiFe_2O_4$/NCNF, $NiFe_2O_4$ bulk and NCNF in 1.0 M KOH solution. (c) The C_{dl} values of the ECSA. (d) The relationship between the TOF values and overpotential at a current density of 10 mA cm^{-2}. (e) Nyquist plots of OP-$NiFe_2O_4$/NCNF, $NiFe_2O_4$/NCNF, $NiFe_2O_4$ bulk, and NCNF. (f) Stability test after 1000 CV cycle and (g) proposed reaction process for OP-$NiFe_2O_4$/NCNF.

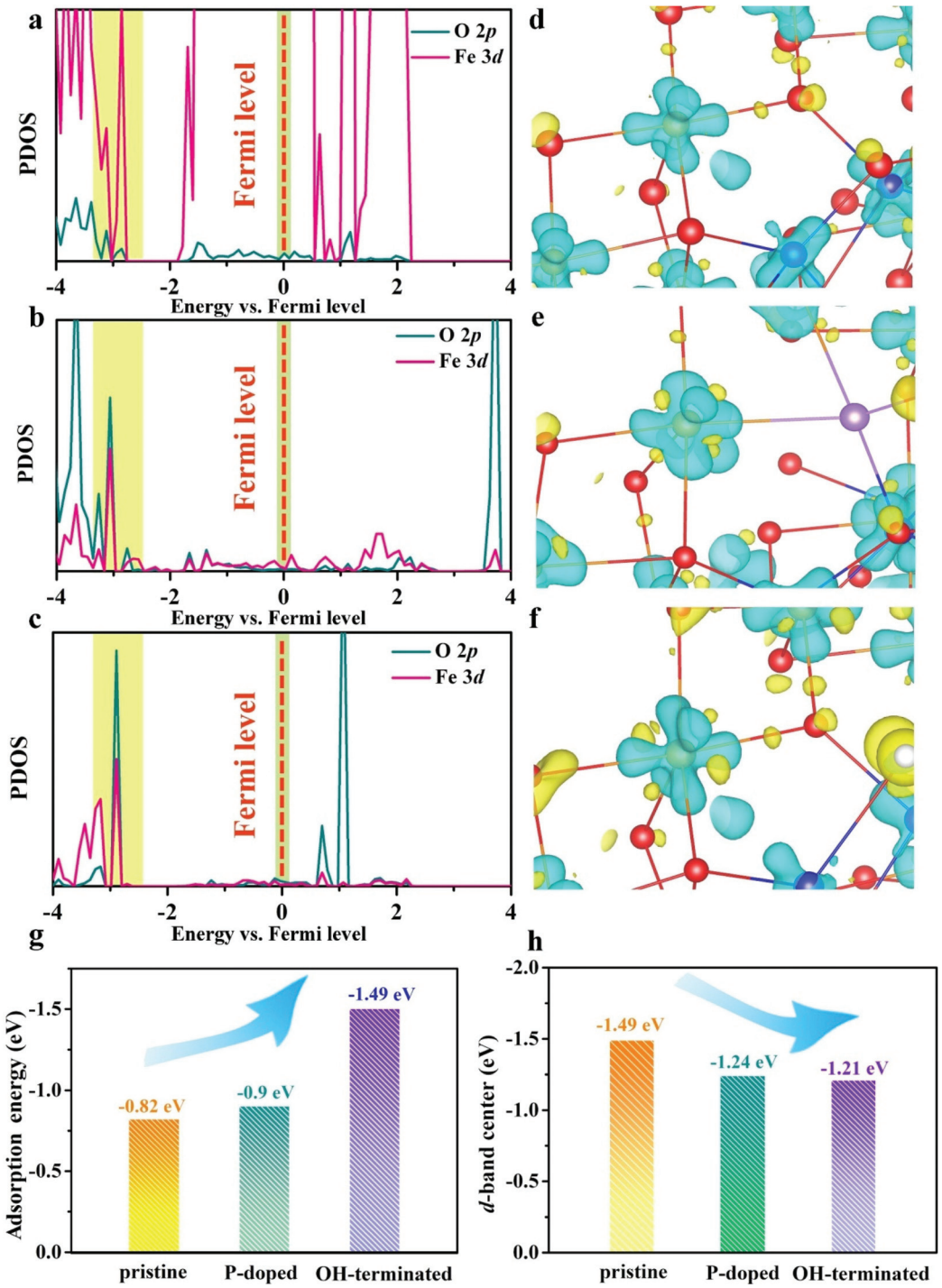

Fig. 5 Calculated PDOS for O 2p and Fe 3d of (a) $NiFe_2O_4$, (b) P-$NiFe_2O_4$, and (c) $NiFe_2O_4$-OH. The Fermi level is set at 0 eV. Corresponding differential charge density of (d) $NiFe_2O_4$, (e) P-$NiFe_2O_4$, and (f) $NiFe_2O_4$-OH. (h) The corresponding calculated adsorption energy for H_2O of $NiFe_2O_4$, P-$NiFe_2O_4$ and $NiFe_2O_4$-OH. (g) The d-band center of $NiFe_2O_4$, P-$NiFe_2O_4$ and $NiFe_2O_4$-OH.

ates. As a result, interaction between the adsorbate and surface is strengthened, which lowers their adsorption free energies for the OER process. These calculation results agree well with the experimental observations and illustrate the positive effect of the introduction of phosphorus and *in situ* formed oxyhydroxide layer for catalyzing the oxygen evolution reaction.

We further implemented this strategy for other multi-transition metal oxides, including $NiCo_2O_4$ and $CoFe_2O_4$ electrocatalyst. As being analogous to the fabrication process of OP-$NiFe_2O_4$/NCNF, both the superficial oxyhydroxide, phosphorus-doped $NiCo_2O_4$ on NCNF (OP-$NiCo_2O_4$/NCNF) and $CoFe_2O_4$ on NCNF (OP-$CoFe_2O_4$/NCNF) were also prepared. As

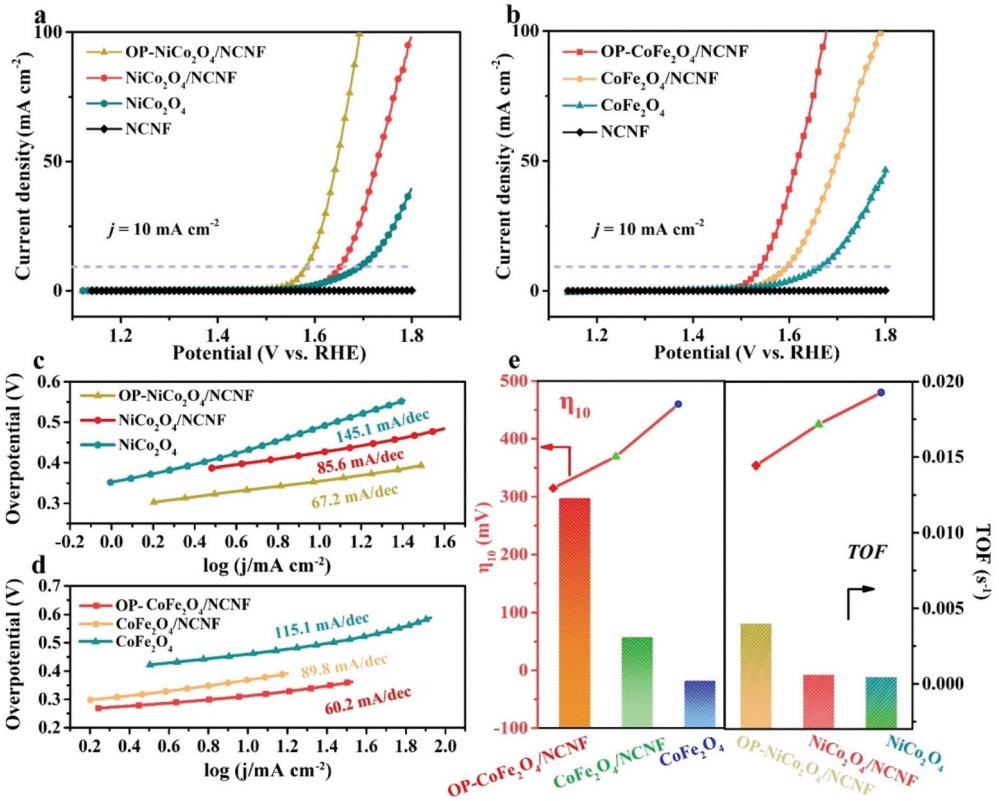

Fig. 6 (a and b) Polarization curves of the oxide nanoarray/NCNF for the oxygen evolution reaction. (c and d) The related Tafel plots. (e) The relationship between the TOF and overpotential at a current density of 10 mA cm^{-2}.

per the XRD patterns (ESI, Fig. S14 and S15†) shown, the obtained multi-transition metal oxides and superficial oxyhydroxide counterparts have close profiles, which match well with the XRD characteristic patterns of $NiCo_2O_4$ (JCPDS no. 20-0781) and $CoFe_2O_4$ (JCPDS no. 03-0864), respectively. As per the SEM images (ESI, Fig. S14 and S15†) shown, both the OP-$NiCo_2O_4$ and OP-$CoFe_2O_4$ are well anchored on the surface of NCNF after phosphorus-doping engineering and electrochemical activation process. From the typical LSV curves in Fig. 6a and b, both OP-$NiCo_2O_4$/NCNF and OP-$CoFe_2O_4$/NCNF show lower overpotential values at current density of 10 mA cm^{-2} as compared to those of the corresponding pristine oxides. Meanwhile, the OP-$NiCo_2O_4$/NCNF and OP-$CoFe_2O_4$/NCNF show not only smaller Tafel slopes but also larger TOF values than the corresponding pristine oxides (Fig. 6c–e). All these results clearly demonstrate that phosphorus-doping engineering and *in situ* superficial self-reconstruction from oxides to amorphous oxyhydroxide layer could be a facile and general method to promote the oxygen evolution reaction performance in transition-metal oxide electrocatalysts.

Conclusion

In summary, we have reported superficial oxyhydroxide, phosphorus-doped $NiFe_2O_4$ nanoarray on nitrogen-doped carbon nanofibers (OP-$NiFe_2O_4$/NCNF) after electrochemical activation process. Depth-profiling analysis from the X-ray photoelectron spectroscopy unveiled that the contents of doped phosphorus atoms increase dynamically from outside to inside of the OP-$NiFe_2O_4$ nanoarray, due to its *in situ* superficial self-reconstruction from oxide to oxyhydroxide. The density functional theory (DFT) calculations revealed that the phosphorus-doping engineering and amorphous oxyhydroxides layer combined to facilitate its adsorption ability towards H_2O molecules with lower energy. As a result, the as-formed superficial oxyhydroxide layers would enhance the oxygen evolution performance of the OP-$NiFe_2O_4$/NCNF with dramatically improved electron transfer ability, which exhibited a low overpotential of 260 mV at the current density of 10 mA cm^{-2}, and a small Tafel slope of 44.8 mV dec^{-1} in alkaline medium. More importantly, we further demonstrated that this is a general method to consistently improve the OER performance in other transition-metal oxide based electrocatalysts. The ability of modulating the local electron density of the catalyst *via* rational surface engineering could hint at a valuable strategy to access high-performance OER catalysts for energy conversion applications.

Conflicts of interest

There are no conflicts to declare.

Acknowledgements

We are really grateful for the financial support from the National Natural Science Foundation of China (51433001, 21674019, 21604010), the Science and Technology Commission of Shanghai Municipality (16520722100), the Program of Shanghai Academic Research Leader (17XD1400100), the "Chenguang Program" supported by Shanghai Education Development Foundation and Shanghai Municipal Education Commission (16CG39). This work was carried out at LvLiang Cloud Computing Center of China, and the calculations were performed on TianHe-2.

References

1 S. Chu and A. Majumdar, *Nature*, 2012, **488**, 294–303.
2 R. Subbaraman, D. Tripkovic, K. C. Chang, D. Strmcnik, A. P. Paulikas, P. Hirunsit, M. Chan, J. Greeley, V. Stamenkovic and N. M. Markovic, *Nat. Mater.*, 2012, **11**, 550–557.
3 Y. Jiao, Y. Zheng, M. Jaroniec and S. Z. Qiao, *Chem. Soc. Rev.*, 2015, **44**, 2060–2086.
4 J. T. Zhang, L. T. Qu, G. Q. Shi, J. Y. Liu, J. F. Chen and L. M. Dai, *Angew. Chem., Int. Ed.*, 2016, **55**, 2230–2234.
5 C. Guo, J. Ran, A. Vasileff and S. Z. Qiao, *Energy Environ. Sci.*, 2018, **11**, 45–56.
6 Z. W. Seh, J. Kibsgaard, C. F. Dickens, I. Chorkendorff, J. K. Nørskov and T. F. Jaramillo, *Science*, 2017, **355**, eaad4998.
7 H. L. Guo, J. Zhou, Q. Q. Li, Y. M. Li, W. Zong, J. X. Zhu, J. S. Xu, C. Zhang and T. X. Liu, *Adv. Funct. Mater.*, 2020, 2000024.
8 J. Yang, J. K. Cooper, F. M. Toma, K. A. Walczak, M. Favaro, J. W. Beeman, L. H. Hess, C. Wang, C. Zhu, S. Gul, J. Yano, C. Kisielowski, A. Schwartzberg and I. D. Sharp, *Nat. Mater.*, 2017, **16**, 335–341.
9 F. L. Lai, N. Chen, X. B. Ye, G. J. He, W. Zong, K. B. Holt, B. C. Pan, I. P. Parkin, R. X. Liu and R. J. Chen, *Adv. Funct. Mater.*, 2020, **30**, 1907376.
10 Y. Pi, Q. Shao, P. Wang, F. Lv, S. Guo, J. Guo and X. Huang, *Angew. Chem., Int. Ed.*, 2017, **56**, 4502–4506.
11 P. Chen, T. Zhou, L. Xing, K. Xu, Y. Tong, H. Xie, L. Zhang, W. Yan, W. Chu, C. Wu and Y. Xie, *Angew. Chem., Int. Ed.*, 2017, **56**, 610–614.
12 L. Zhang, Y. Jia, G. Gao, X. Yan, N. Chen, J. Chen, M. T. Soo, B. Wood, D. Yang, A. Du and X. Yao, *Chem*, 2018, **4**, 285–297.
13 N. T. Suen, S. F. Hung, Q. Quan, N. Zhang, Y. J. Xu and H. M. Chen, *Chem. Soc. Rev.*, 2017, **46**, 337–365.
14 Z. F. Huang, J. Wang, Y. C. Peng, C. Y. Jung, A. Fisher and X. Wang, *Adv. Energy Mater.*, 2017, **7**, 1700544.
15 K. Obata and K. Takanabe, *Angew. Chem., Int. Ed.*, 2018, **130**, 1632–1636.
16 T. Audichon, T. W. Napporn, C. Canaff, U. C. Morais, M. C. Comminges and K. B. Kokoh, *J. Phys. Chem. C*, 2016, **120**, 2562–2573.
17 J. Feng, F. Lv, W. Zhang, P. Li, K. Wang, C. Yang, B. Wang, Y. Yang, J. Zhou, F. Lin, G. C. Wang and S. Guo, *Adv. Mater.*, 2017, **29**, 1703798.
18 X. Han, C. Yu, S. Zhou, C. Zhao, H. Huang, J. Yang, Z. Liu, J. Zhao and J. Qiu, *Adv. Energy Mater.*, 2017, **7**, 1602148.
19 Y. Jia, L. Z. Zhang, G. P. Gao, H. Chen, B. Wang, J. Z. Zhou, M. T. Soo, M. Hong, X. C. Yan, G. G. Qian, J. Zou, A. J. Du and X. D. Yao, *Adv. Mater.*, 2017, **29**, 1700017.
20 S. Dou, C. L. Dong, Z. Hu, Y. C. Huang, J. L. Chen, L. Tao, D. Yan, D. Chen, S. Shen and S. Chou, *Adv. Funct. Mater.*, 2017, **27**, 1702546.
21 J. Yin, Y. Li, F. Lv, M. Lu, K. Sun, W. Wang, L. Wang, F. Cheng, Y. Li, P. Xi and S. Guo, *Adv. Mater.*, 2017, **29**, 1704681.
22 Z. W. Fang, L. L. Peng, H. F. Lv, Y. Zhu, C. S. Yan, S. Q. Wang, P. Kalyani, X. J. Wu and G. H. Yu, *ACS Nano*, 2017, **11**, 9550–9557.
23 M. Wang, M. Lin, J. Li, L. Huang, Z. Zhuang, C. Lin, L. Zhou and L. Mai, *Chem. Commun.*, 2017, **53**, 8372–8375.
24 J. Liu, D. Zhu, T. Ling, A. Vasileff and S. Z. Qiao, *Nano Energy*, 2017, **40**, 264–273.
25 Y. Ha, L. Shi, X. Yan, Z. Chen, Y. Li, W. Xu and R. Wu, *ACS Appl. Mater. Interfaces*, 2019, **11**, 45546–45553.
26 B. You, M. T. Tang, C. Tsai, F. Abild-Pedersen, X. Zheng and H. Li, *Adv. Mater.*, 2019, **31**, 1807001.
27 S. H. Hsu, S. F. Hung, H. Y. Wang, F. X. Xiao, L. Zhang, H. Yang, H. M. Chen, J. M. Lee and B. Liu, *Small Methods*, 2018, **2**, 1800001.
28 L. Zhuang, L. Ge, Y. Yang, M. Li, Y. Jia, X. Yao and Z. Zhu, *Adv. Mater.*, 2017, **29**, 1606793.
29 J. Bao, X. Zhang, B. Fan, J. Zhang, M. Zhou, W. Yang, X. Hu, H. Wang, B. Pan and Y. Xie, *Angew. Chem., Int. Ed.*, 2015, **54**, 7399–7404.
30 X. Wang, L. Zhuang, Y. Jia, H. Liu, X. Yan, L. Zhang, D. Yang, Z. Zhu and X. Yao, *Angew. Chem., Int. Ed.*, 2018, **57**, 16421–16425.
31 Y. Zhu, H. C. Chen, C. S. Hsu, T. S. Lin, C. J. Chang, S. C. Chang, L. D. Tsai and H. M. Chen, *ACS Energy Lett.*, 2019, **4**, 987–994.
32 Z. Xiao, Y. Wang, Y. C. Huang, Z. Wei, C. L. Dong, J. Ma, S. Shen, Y. Li and S. Wang, *Energy Environ. Sci.*, 2017, **10**, 2563–2569.
33 P. Liu, J. Zhu, J. Zhang, P. Xi, K. Tao, D. Gao and D. Xue, *ACS Energy Lett.*, 2017, **2**, 745–752.
34 T. Wu, S. Sun, J. Song, S. Xi, Y. Du, B. Chen, W. A. Sasangka, H. Liao, C. L. Gan, G. G. Scherer, L. Zeng, H. Wang, H. Li, A. Grimaud and Z. J. Xu, *Nat. Catal.*, 2019, **2**, 763–772.
35 X. Xu, F. Song and X. Hu, *Nat. Commun.*, 2016, **7**, 12324.
36 H. J. Zhang, X. P. Li, A. Hahnel, V. Naumann, C. Lin, S. Azimi, S. L. Schweizer, W. Maijenburg and R. B. Wehrspohn, *Adv. Funct. Mater.*, 2018, **28**, 1706847.

37 Y. Duan, Z. Y. Yu, S. J. Hu, X. S. Zheng, C. T. Zhang, H. H. Ding, B. C. Hu, Q. Q. Fu, Z. L. Yu, X. Zheng, J. F. Zhu, M. R. Gao and S. H. Yu, *Angew. Chem.*, 2019, **131**, 15919–15924.
38 X. Y. Yu, Y. Feng, B. Guan, X. W. D. Lou and U. Paik, *Energy Environ. Sci.*, 2016, **9**, 1246–1250.
39 S. Chen, J. Duan, M. Jaroniec and S. Z. Qiao, *Adv. Mater.*, 2014, **26**, 2925–2930.
40 Z. X. Pei, H. F. Li, Y. Huang, Q. Xue, Y. Huang, M. S. Zhu, Z. Wang and C. Y. Zhi, *Energy Environ. Sci.*, 2017, **10**, 742–749.
41 F. L. Lai, J. R. Feng, T. Heil, G. C. Wang, P. Adler, M. Antonietti and M. Oschatz, *Energy Storage Mater.*, 2019, **20**, 188–195.
42 M. Yu, Z. Wang, C. Hou, Z. Wang, C. Liang, C. Zhao, Y. Tong, X. Lu and S. Yang, *Adv. Mater.*, 2017, **29**, 1602868.
43 X. L. Ning, F. Li, Y. Zhou, Y. E. Miao, C. Wei and T. X. Liu, *Chem. Eng. J.*, 2017, **328**, 599–608.
44 F. L. Lai, J. R. Feng, X. B. Ye, W. Zong, G. J. He, Y. E. Miao, X. M. Han, X. Y. Ling, I. P. Parkin, B. C. Pan, Y. F. Sun and T. X. Liu, *J. Mater. Chem. A*, 2019, **7**, 827–833.
45 X. Zheng, B. Zhang, P. DeLuna, Y. Liang, R. Comin, O. Voznyy, L. Han, F. P. G. de Arquer, M. Liu, C. T. Dinh, T. Regier, J. J. Dynes, S. S. He, H. L. L. Xin, H. S. Peng, D. Prendergast, X. W. Du and E. H. Sargent, *Nat. Chem.*, 2018, **10**, 149–154.
46 G. Liu, K. Wang, X. Gao, D. He and J. Li, *Electrochim. Acta*, 2016, **211**, 871–878.
47 S. Anantharaj, K. Karthick, M. Venkatesh, T. V. S. V. Simha, A. S. Salunke, L. Ma, H. Liang and S. Kundu, *Nano Energy*, 2017, **39**, 30–43.
48 P. Chen, T. Zhou, S. Wang, N. Zhang, Y. Tong, H. Ju, W. Chu, C. Wu and Y. Xie, *Angew. Chem., Int. Ed.*, 2018, **57**, 15471–15475.
49 W. Zong, F. L. Lai, G. J. He, J. R. Feng, W. Wang, R. Q. Lian, Y. E. Miao, G. C. Wang, I. P. Parkin and T. X. Liu, *Small*, 2018, **14**, 1801562.